Quasi-monochromatic ULF foreshock waves as observed by the four-spacecraft Cluster mission: 2. Oblique propagation

J. P. Eastwood

Laboratory for Solar and Space Physics, Geospace Physics Branch, NASA Goddard Space Flight Center, Greenbelt, Maryland, USA

A. Balogh and E. A. Lucek

Space and Atmospheric Physics, Blackett Laboratory, Imperial College London, London, UK

C. Mazelle and I. Dandouras

Centre d'Etude Spatiale des Rayonnements, Centre National de la Recherche Scientifique, Toulouse, France

[1]   This paper presents the results of a statistical investigation into the nature of oblique wave propagation in the foreshock. Observations have shown that foreshock ULF waves tend to propagate obliquely to the background magnetic field. This is in contrast to theoretical work, which predicts that the growth rate of the mechanism responsible for the waves is maximized for parallel propagation, at least in the linear regime in homogenous plasma. Here we use data from the Cluster mission to study in detail the oblique propagation of a particular class of foreshock ULF wave, the 30 s quasi-monochromatic wave. We find that these waves persistently propagate at oblique angles to the magnetic field. Over the whole data set, the average value of θ_{kB} was found to be $21 \pm 14°$. Oblique propagation is observed even when the interplanetary magnetic field (IMF) cone angle is small, such that the convective component of the solar wind velocity, $v_{E \times B}$, is comparable to the wave speed. In this subset of the data, the mean value of θ_{kB} was $12.9 \pm 7.1°$. In the subset of data for which the IMF cone angle exceeded $45°$, the mean value of θ_{kB} was $19.5 \pm 10.7°$. When the angle between the IMF and the x geocentric solar ecliptic (GSE) direction (i.e., the solar wind vector) is large, the wave k vectors tend to be confined in the plane defined by the x GSE direction and the magnetic field and a systematic deflection is observed. The dependence of θ_{kB} on $v_{E \times B}$ is also studied.

1.   Introduction

[2]   Upstream of the collisionless bow shock generated by the interaction of the solar wind with the Earth's magnetic field, there exists a volume of space filled with backstreaming particles and associated wave activity. This region, known as the foreshock, is extremely complex and exhibits a wide variety of behaviors. Its dynamics depend on the interaction of the backstreaming particles with the solar wind; as such, it is an excellent natural arena for the study of beam instabilities in collisionless plasmas. Although a great deal of progress has been made (see, e.g., Advances in Space Research, 15(8/9), 1995, and references therein), a number of issues remain. Here we will consider one problem in particular, the nature of oblique ultra-low-frequency (ULF) wave propagation in the foreshock.

[3]   Several different types of ion distribution have been identified in the foreshock; field-aligned, intermediate, gyrotropic, gyrophase bunched, and diffuse [e.g., *Fuselier*, 1994, 1995]. Similarly, several different types of wave have been observed: 30 s quasi-monochromatic, shocklets and discrete wave packets (also referred to as steepened waves or fully developed wave activity), 1 Hz waves, 3 s waves [e.g., *Le and Russell*, 1994; *Greenstadt et al.*, 1995; *Burgess*, 1997], and more recently 10 s waves [*Eastwood et al.*, 2003]. We will not discuss the 1 Hz, 3 s, or 10 s waves further here. This complexity is partly explained by the shock itself. Field-aligned distributions are thought to result from ion reflection or leakage processes at the quasi-perpendicular shock [*Sonnerup*, 1969; *Tanaka et al.*, 1983; *Schwartz and Burgess*, 1984; *Möbius et al.*, 2001]. Intermediate distributions may arise through leakage from the magnetosheath [*Edmiston et al.*, 1982] and diffuse distributions from processes associated with the quasi-parallel

shock [e.g., *Scholer*, 1995]. The quasi-parallel shock also specularly reflects ions [*Gosling et al.*, 1982], potentially leading to the production of gyrophase-bunched distributions [*Gurgiolo et al.*, 1983].

[4] A second source of complexity arises from wave-particle interactions occurring in the foreshock itself. In the most general terms, the backstreaming ions are responsible for the generation of the low-frequency waves observed in the foreshock [*Barnes*, 1970]. In fact, the combination of backstreaming ions and solar wind is potentially subject to several instabilities, depending on the properties of the backstreaming beam. Linear analysis reveals that fast, cold, rarified beams are primarily subject to the ion-ion right-hand resonant cyclotron beam instability, leading to the production of right-hand polarized magnetosonic waves propagating parallel to the beam. If the beam is sufficiently hot and slow, the growth rate of the ion-ion left-hand resonant instability is increased and this mode emerges as a left-hand polarized Alfvén/ion cyclotron wave again propagating parallel to the beam. If the backstreaming beam is cool, and sufficiently dense and fast moving, an ion-ion nonresonant instability occurs, which is right-handed and propagates antiparallel to the beam [*Gary*, 1993; *Treumann and Baumjohann*, 1996].

[5] Neither quasi-monochromatic ULF waves nor shocklets are observed in conjunction with field-aligned distributions [*Paschmann et al.*, 1979]. The 30 s period quasi-monochromatic waves are observed in conjunction with intermediate, gyrotropic and/or gyrophase bunched distributions, and shocklets and discrete wave packets are observed in conjunction with diffuse distributions [*Hoppe et al.*, 1981]. Single spacecraft analysis of the 30 s period quasi-monochromatic ULF waves showed that they are predominantly left-handed in the spacecraft frame [*Fairfield*, 1969] and are slightly compressive. Using data from ISEE 1 and 2, *Hoppe and Russell* [1983] established on the basis of case studies that 30 s period waves observed to be left-handed in the spacecraft frame were propagating sunward in the solar wind rest frame, away from the shock and in the same direction as the backstreaming ion beams.

[6] On the basis of these observations, and given the fact that field-aligned distributions are primarily subject to the ion-ion right-hand resonant instability [*Gary et al.*, 1981], it was proposed that field-aligned distributions were responsible for the generation of 30 s period waves. These waves were then thought to scatter the field-aligned beam into an intermediate-type distribution [*Winske and Leroy*, 1984; *Thomsen*, 1985; *Winske and Quest*, 1986] or trap the beam forming gyrophase bunched distributions [*Hoshino and Terasawa*, 1985; *Mazelle et al.*, 2000; *Meziane et al.*, 2001; *Mazelle et al.*, 2003]. It has also been proposed, and observed, that these waves might be generated by gyrating distributions directly, for example by those produced at the quasi-parallel shock [*Thomsen et al.*, 1985; *Fuselier et al.*, 1986].

[7] The shocklets resemble steepened 30 s waves, driving leading whistler wave trains (the discrete wave packets), and are observed in conjunction with diffuse ion distributions [*Hoppe et al.*, 1981; *Elaoufir et al.*, 1990]. A particular property of shocklets is that they are compressive. Oblique propagation is necessary to account for the observed steepened waveforms and magnetic field polarizations of shock-lets [e.g., *Hoppe and Russell*, 1983; *Le and Russell*, 1994]. Shocklets are linearly polarized, which precludes the use of single and dual spacecraft techniques to determine their propagation direction [*Song and Russell*, 1999]. The discrete wave packets are circularly polarized [*Hoppe et al.*, 1981; *Elaoufir et al.*, 1990]; studies applying minimum variance analysis (MVA) to observations of discrete wave packets have shown that they propagate obliquely to the field (e.g., $\theta_{kB} = 28°$ [*Hoppe et al.*, 1981] and $\theta_{kB} = 45°$ [*Elaoufir et al.*, 1990]).

[8] Oblique propagation is not restricted to shocklets. The 30 s foreshock ULF waves have also been observed to propagate obliquely to the magnetic field, although the experimental data is sparse and is derived from a small number of case studies. For example, in case studies applying MVA to ISEE observations of 30 s waves, $\theta_{kB} \sim 20°$ was reported [*Hoppe et al.*, 1981]. Cluster case studies have found similar values of θ_{kB} [*Eastwood et al.*, 2002; *Narita et al.*, 2003; *Eastwood et al.*, 2004]. Observations of such waves associated with gyrating distributions also found significant oblique propagation [*Meziane et al.*, 2001], although θ_{kB} can be small [*Meziane et al.*, 1997; *Mazelle et al.*, 2003].

[9] Linear analysis reveals that the growth rate of the ion-ion right-hand resonant instability is maximized for parallel propagation for beam parameters corresponding to those typically observed [*Gary et al.*, 1981; *Gary*, 1993]. Although in other regions of parameter space, particularly corresponding to the fast solar wind, growth rates can be maximized for obliquely propagating modes [*Daughton and Gary*, 1998], the discrepancy between these calculations using foreshock parameters and observations suggests that the nonlinear phase cannot be ignored. Furthermore, such analyses usually assume that the background plasma conditions are spatially uniform and time invariant.

[10] To understand this, computer simulations have been used to study the nonlinear evolution of the beam-plasma interaction. Early one- and two-dimensional hybrid (particle ions, fluid electrons) simulations showed that the initial field-aligned beam (beam density $n_b = 0.015 \times$ the core (solar wind) density n_p) excited right-hand polarized waves which then pitch angle scattered the beam into a "diffuse" ion distribution. The parallel propagating waves did not steepen into shocklets [*Winske and Leroy*, 1984; *Winske and Quest*, 1986]. It was also concluded that one-dimensional simulations retained the principal features of the two-dimensional simulations. (However, compositional evidence suggests that field-aligned distributions are not the primary source of diffuse distributions in the foreshock. Field-aligned distributions consist mainly of protons, whereas diffuse distributions contain solar wind concentrations of He^{++} [e.g., *Fuselier*, 1994]). One-dimensional numerical simulations of the same system using a full particle code showed that after generating the waves, the waves caused the beam ions to bunch in phase space, leading to gyrophase bunching of the beam distribution before further scattering occurred later in the simulation [*Hoshino and Terasawa*, 1985].

[11] *Hada et al.* [1987] solved the linear dispersion relation for electromagnetic waves in the presence of both field-aligned beams and diffuse beams and found that in both cases the growth rate was maximized for parallel
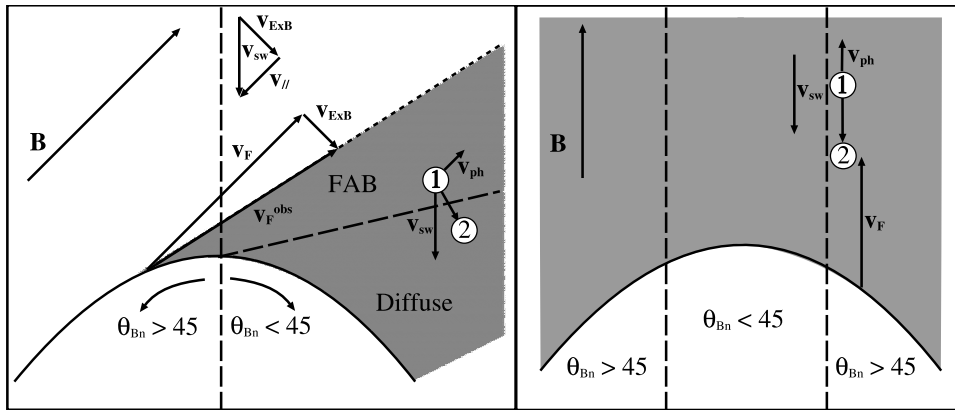
Figure 1. The idealized morphology of the foreshock is shown for two different interplanetary magnetic field (IMF) orientations. The left-hand panel shows the foreshock when the IMF is aligned to the Parker spiral. The right-hand panel shows the foreshock when the IMF is radial. The extent of the foreshock is shown in gray. In each case, waves generated at point 1 are later found at point 2.

propagation. The wave phase speed was found to be larger in the field-aligned beam region than in the diffuse beam region. Hada et al. also found that the growth rate in the presence of diffuse ions was not large enough for the waves to reach large amplitudes before being convected out of the foreshock. In particular, they concluded that the steepened waves could not be generated in the diffuse ion foreshock itself.

[12] They suggested that parallel-propagating waves growing in the field-aligned and intermediate regions of the foreshock would refract as they were carried into the diffuse ion foreshock by the solar wind. The left-hand panel of Figure 1 shows the idealized configuration of the foreshock for $\theta_{Bx} = 45°$; $\theta_{Bx} = acos(B_x/B)$ is the cone angle of the interplanetary magnetic field (IMF). The coordinate system [x, y, z] refers to the geocentric solar ecliptic (GSE) coordinate system. The shock is the curved surface at the bottom of the figure and is quasi-perpendicular (parallel) on the left- (right-) hand side. The solar wind flows down the page. The leading edge of the ion foreshock is defined by the trajectory of the backstreaming field aligned beams upstream of the quasi-perpendicular shock, injected with velocity $\mathbf{v_F}$. As the ions move back into the upstream region, they are subject to $\mathbf{E} \times \mathbf{B}$ drift in the solar wind convection electric field, and consequently, the ion foreshock boundary is not field-aligned. The gray region corresponds to the ion foreshock. Within the ion foreshock, diffuse ions are confined to the region upstream of the quasi-parallel shock [Bonifazi and Moreno, 1981].

[13] ULF waves generated by field-aligned distributions at point 1 (circled) attempt to propagate upstream with velocity $\mathbf{v_{ph}}$. However, they are convected antisunward by the solar wind to point 2 (circled) in the diffuse ion foreshock. To estimate the amount of refraction ($\Delta\theta_{kB}$), Hada et al. [1987] took a magnetic field cone angle of 45°, a ULF wave phase speed of $2V_A$ in the "reflected" ion foreshock and V_A in the diffuse ion foreshock (where V_A is the Alfvén speed), and a solar wind speed of $8V_A$. They found $\Delta\theta_{kB} \sim 10°$ in the $\mathbf{v_{sw}} - \mathbf{B}$ plane. Hada et al. [1987] also simulated the evolution of obliquely propagating waves, showing that they would steepen relatively quickly.

[14] Other one-dimensional hybrid MHD simulations of obliquely propagating ULF waves were also carried out, showing that such obliquely propagating waves are dispersive and that an initially coherent steepened ULF wave degenerates into a discrete wave packet and a shocklet which behaves as a subcritical dispersive shock [Omidi and Winske, 1998, 1990]. Elaoufir et al. [1990] used MVA to study ISEE observations of discrete wave packets. It was shown that statistically, there was a deviation of the discrete wave packets in the plane defined by the magnetic field and the solar wind. It was concluded that the oblique propagation of the shocklets was qualitatively consistent with the refraction mechanism proposed by Hada et al. [1987]. A semiquantitative analysis was also shown to be consistent with the model.

[15] However, it has since been pointed out that this model cannot explain all observations of obliquely propagating discrete wave packets and shocklets. In particular, as discussed by Le and Russell [1994], this model breaks down when the interplanetary magnetic field is radial. This is illustrated in the right-hand panel of Figure 1, which shows the idealized morphology of the foreshock for radial IMF conditions. The central region of the shock is quasi-parallel in nature whereas the flanks of the shock are quasi-perpendicular. The subsolar upstream region is filled with backstreaming particles and ULF waves [Le and Russell, 1994]. Since the solar wind convection electric field is small, waves will not be transported through different regions of the foreshock as in the first case. Consequently, one might expect that shocklets and discrete wave packets would not develop. However, such waves are observed when the IMF is radial [Le and Russell, 1994]. We are unaware of any quantitative experimental studies that specifically examined the oblique propagation of ULF waves under radial IMF conditions.

[16] Further work on this problem has largely relied on numerical investigations. Akimoto et al. [1991, 1993] studied the generation of magnetic pulsations using one-dimensional hybrid simulations, particularly examining which modes contributed to their growth. Hellinger and Mangeney [1999] extended early simulations [Winske and Leroy, 1984; Winske and Quest, 1986] by conducting a two-dimensional

simulation of a denser backstreaming beam ($n_b/n_p = 0.04$). They observed filamentation of the beam and pulses in magnetic field strength. Linear analysis revealed a local maximum in the growth rate for strongly oblique propagation, which gave rise to beam filamentation. *Kucharek et al.* [2000] performed three-dimensional simulations to study cross field diffusion in the wave field but not to examine the oblique propagation of waves specifically. Finally, *Wang and Lin* [2003] have performed one- and two-dimensional hybrid simulations in order to study the oblique propagation of different wave modes in the nonlinear regime, for different beam parameters. Their two-dimensional weak beam case produced oblique pulsations similar to those reported by *Hellinger and Mangeney* [1999].

[17] In addition to these simulations examining the beam/plasma interaction, shock simulations have also revealed relevant wave dynamics. In particular, two-dimensional simulations of the quasi-parallel shock have shown that waves are refracted in the region of large diffuse ion gradients close to the shock [*Krauss-Varban and Omidi*, 1993; *Scholer et al.*, 1993]. It was observed that initially field-aligned waves were refracted into a direction parallel to the backstreaming density gradient, that is, parallel to the shock normal. This effect was confined to the plane of the simulation, defined by the solar wind and the magnetic field.

[18] Quantitative experimental investigations into oblique propagation, which would complement these extensive numerical investigations, remain somewhat sparse. Single and dual spacecraft analysis of shocklets has been limited by the fact that MVA cannot be used to study linearly polarized waves [e.g., *Song and Russell*, 1999]. Studies of discrete wave packets have been published [*Hoppe et al.*, 1981; *Elaoufir et al.*, 1990], as discussed above. Only limited quantitative information about the oblique propagation of the 30 s waves has been presented [*Hoppe et al.*, 1981; *Eastwood et al.*, 2002].

[19] More recently, *Eastwood et al.* [2004] presented the results of a case study specifically investigating the oblique propagation of 30 s waves for large IMF cone angle ($\theta_{Bx} = 70°$). Using Cluster multispacecraft data and techniques, they found a significant deviation of the average wave k vector away from the magnetic field in the plane defined by the magnetic field and the x_{GSE} direction. The observations presented by Eastwood et al. most likely correspond to waves growing to their observed amplitude in the presence of intermediate and/or gyrating distributions.

[20] More comprehensive observations are required to fully characterize the problem of oblique propagation and to guide the development of both simulations and nonlinear theory. The availability of four spacecraft data from the Cluster mission [*Escoubet et al.*, 2001] allows the propagation direction of waves to be calculated using new techniques that are less restrictive. Cluster therefore represents an excellent opportunity to study this problem. To better understand the nature of oblique wave propagation in the foreshock, we used Cluster data in combination with multispacecraft analysis to investigate the oblique propagation of 30 s waves; the class of waves for which the least amount of experimental data is currently available. These data have also been used to conduct a more general investigation characterizing the wave properties and investigating the

experimental nature of the beam resonance condition responsible for their generation [*Eastwood et al.*, 2005]. The full details of the data selection and analysis procedures are given by *Eastwood et al.* [2005], but in the next section the relevant points are summarized for completeness. In section 3, the experimental observations are presented. The observations are discussed in section 4, and in section 5 conclusions are presented, together with unresolved issues and suggestions for development of the work.

2. Data Analysis

[21] Cluster magnetic field data measured by the fluxgate magnetometers (FGM) [*Balogh et al.*, 2001] obtained during the first dayside pass in 2001 were examined for intervals of foreshock wave activity. During this time, the separation of the spacecraft was ∼600 km. During the second and third dayside passes, the separations were ∼100 km and ∼6000 km; it was felt that the 100 km separations were potentially too small to reliably determine wave properties and that the 6000 km separations were potentially too large to prevent spatial aliasing.

[22] Thirty one separate intervals of quasi-monochromatic ULF wave activity on 12 different days were identified for analysis. Figure 2 shows the orbits from which data was used. This figure can also be found in the work of *Eastwood et al.* [2005] and is included here for completeness. The orbit is shown in gray projected into the x-y GSE plane (left) and the x-z GSE plane (right). The black dashed line represents a cut through the surface of a nominal bow shock (based on the *Peredo et al.* [1995] model) in these planes. The sections of the orbit emboldened in black represent intervals of analyzed foreshock wave activity. Contained in this data set are the observations previously analyzed by *Eastwood et al.* [2004].

[23] These intervals were filtered to remove high-frequency signatures and divided into 2-min subintervals. This time length was chosen as being long enough for analysis, but short enough to assume stationarity in the background parameters. Although the solar wind speed was relatively stable, the background magnetic field orientation and strength were observed to change on timescales of minutes, as was the density. Also we observed that the wave profile and/or amplitude would change on the same timescale and that on occasion the waves would disappear for a few cycles. In the foreshock, we expect that the position of the shock is constantly changing [e.g., *Maksimovic et al.*, 2003] and that the properties of the backstreaming ions (e.g., fluxes) may therefore be time-dependent. Furthermore, the waves are locally growing and saturating, and the backstreaming ions are interacting with the waves. This also influenced our decision to examine shorter subintervals. Subintervals were then discarded if they contained data gaps.

[24] For each subinterval, the data from each spacecraft were transformed into the spacecraft 1 variance coordinate system. The transformed spacecraft time series were then cross-correlated [*Bendat and Piersol*, 1986], resulting in a set of time differences; these time differences were then used to find the orientation of the wave front from a timing analysis [e.g., *Schwartz*, 1998]. Plasma data from the Cluster Ion Spectrometry (CIS) Hot Ion Analyzer (HIA)
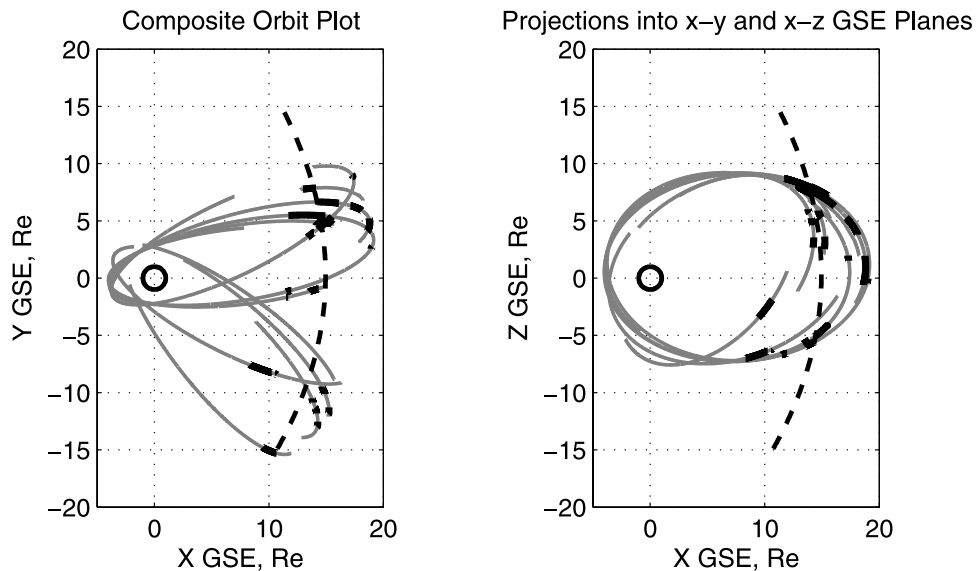
Figure 2. Intervals of foreshock observations forming basis of statistical analysis. The orbit is shown in gray projected into (left) the x-y geocentric solar ecliptic (GSE) plane and (right) the x-z GSE plane. The black dashed line represents a cut through the surface of a nominal bow shock in these planes. The sections of the orbit emboldened in black represent intervals of analysed foreshock wave activity.

operating in solar wind modes were used to find the local solar wind properties [*Rème et al.*, 2001]. The wavelength and wave front orientation are frame-independent and can therefore be found directly from spacecraft frame measurements, without applying a Doppler shift. The error in the estimate of wave vector orientation is of the order of a few degrees. This procedure resulted in a sample of 255 2-min observations of quasi-monochromatic ULF wave activity, covering a wide range of upstream conditions. In the work of *Eastwood et al.* [2005], more details are given concerning the analysis technique, in particular concerning how all the properties of the waves were found. Here, we are concerned just with the orientation of the *k* vector. Finally, we note that we did not average the shorter intervals back over the longer intervals, as it was not easy to establish that the foreshock was behaving in a time stationary and homogenous manner, particularly given that instabilities are growing and locally saturating, that the waves are evolving, and that the particle input to the foreshock is time-dependent, since the position of the shock changes and its structure is not time-independent.
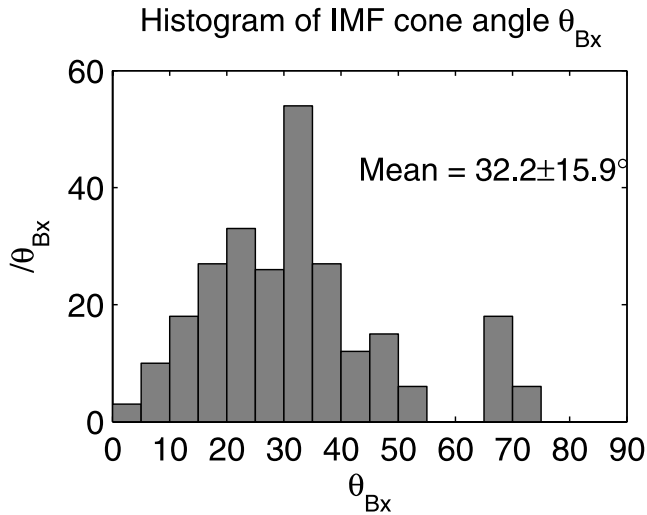
3. Experimental Observations

[25] Using the data discussed in section 2, θ_{kB} was calculated for each sample. The histogram of θ_{kB} is shown in Figure 3. Note that θ_{kB} has been forced to lie between 0 and 90°; if this condition is not enforced, one obtains an essentially symmetric histogram between 0 and 180°. In doing this, it is assumed that the actual direction of the magnetic field is not as important as its alignment (if the field is radial, we are not immediately concerned by whether it points toward or away from the Sun). The angular error in any single estimate of *k* vector orientation is of the order of a few degrees. Over the whole dataset, the average value of θ_{kB} was found to be $21 \pm 14°$. This is consistent with previous measurements based on individual case studies

[e.g., *Hoppe et al.*, 1981]. The data were examined to see if θ_{kB} scaled with solar wind density, speed, or magnetic field strength. None of these parameters were seen to control θ_{kB}. Furthermore, no correlation was seen between θ_{kB} and either the wavelength or period of the waves. These observations cover a range of θ_{Bx}. The histogram of θ_{Bx} is shown in Figure 4. The mean value of θ_{Bx} was found to be $32.2 \pm 15.9°$. Figure 5 shows a two-dimensional histogram of the data binned in θ_{Bx} and θ_{kB}. The color scale indicates the number of samples in each bin. The modal bin (n = 13) is centered on $\theta_{Bx} = 32.5°$ and $\theta_{kB} = 17.5°$. Figure 5 shows that as θ_{Bx} increases from 0 to ~45°, the maximum observed
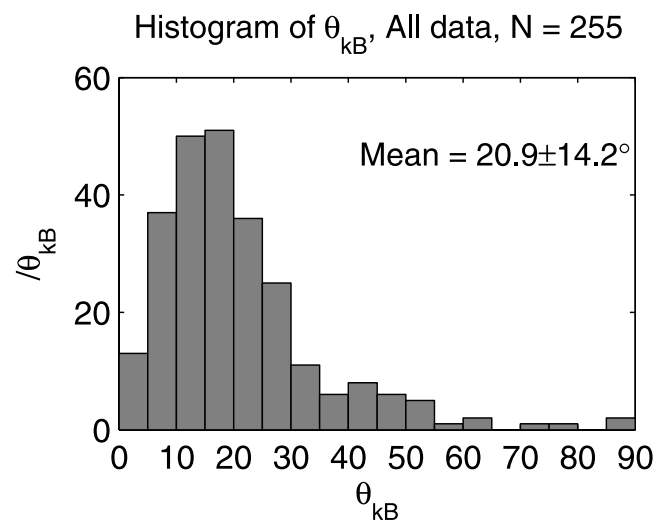
Figure 3. Histogram showing the oblique propagation of quasi-monochromatic foreshock waves. For each sample, the angle θ_{kB} was calculated. The mean value of θ_{kB} was found to be 20.9°.

Histogram of IMF cone angle θ_{Bx}

Figure 4. Histogram of θ_{Bx}. The mean value of θ_{Bx} was found to be 32.2°.

2d histogram – θ_{Bx} and θ_{kB}

Figure 5. Two-dimensional histogram of θ_{Bx} and θ_{kB}. The data were placed into 5° wide bins in both θ_{Bx} and θ_{kB}. The color scale is used to represent the number density in each bin.

value of θ_{kB} also increases. However, even when θ_{Bx} is small, θ_{kB} is significantly nonzero.

[26] To better quantify this, Figure 6 shows the local geometry in the foreshock. In this figure waves propagate to first order along the magnetic field **B** with phase velocity $\mathbf{v_{ph}}$ in the solar wind rest frame. Note that they are shown to propagate parallel to the field for simplicity. The cone angle θ_{Bx} gives the angular separation of the solar wind vector $\mathbf{v_{sw}}$ from the magnetic field **B**, if the solar wind is taken to flow antiparallel to **x**. The solar wind may be decomposed into parallel ($\mathbf{v_{\parallel}}$) and perpendicular ($\mathbf{v_{E \times B}}$) components. If $v_{E \times B} \ll v_{ph}$, convective effects are minimized. We may explore this by considering a limiting value of θ_{Bx} where $v_{E \times B} = v_{ph}$, shown in equation (1):

$$\theta_{Bx} = \sin^{-1}\left(\frac{v_{E \times B}}{v_{sw}}\right) = \sin^{-1}\left(\frac{v_{ph}}{v_{sw}}\right). \qquad (1)$$

In this data set, the average solar wind speed was 424 km s^{-1}, and the average wave phase speed in the solar wind rest frame was ~70 km s^{-1}. This corresponds to $\theta_{Bx} \sim 10°$. If $\theta_{Bx} = 45°$, then the average convective component of the solar wind would be $v_{E \times B} = 424 \sin(45°) = 300$ km s^{-1}. In this case, we would expect the waves to be convected across the magnetic field relatively quickly. Each observed cone angle was compared to the measured solar wind speed and the calculated wave phase speed based on equation (1). Strictly speaking, it may be said that $v_{E \times B}$ should be compared to the parallel component of the phase velocity. However, if $\theta_{kB} \sim 20°$, this leads to a 5% error in v_{ph}, which is less than the error in the individual calculations of v_{ph} [*Eastwood et al.*, 2005]; this does not induce a significant change in the results. If the observed cone angle was found to be less than the cone angle required for $v_{E \times B} = v_{ph}$, the sample was retained. There were 14 such samples identified, with a mean cone angle of 8.7°. The mean value of θ_{kB} was 12.9 ± 7.1°. In comparison, 45 intervals were identified with $\theta_{Bx} > 45°$, with a mean value of $\theta_{kB} = 19.5 \pm 10.7°$. The remaining 196 samples, with $\theta_{Bx} < 45°$ but larger than the cone angle limit described above had a mean value of $\theta_{kB} = 21.7 \pm 15.1°$.
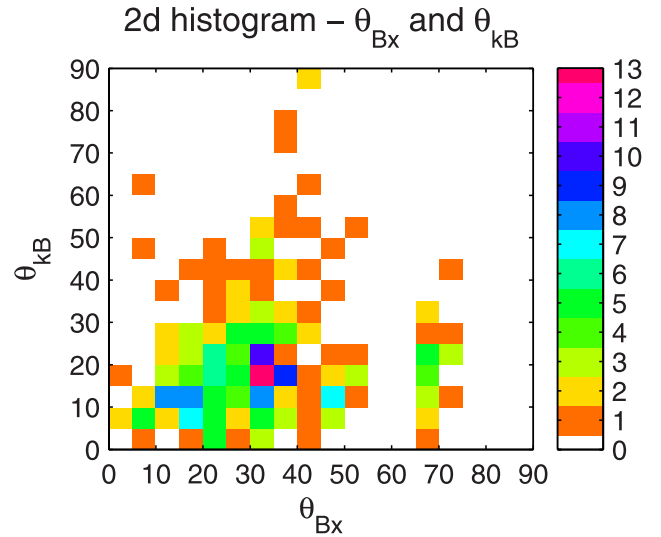
[27] The data were studied in more detail to clarify the relationship between the IMF cone angle θ_{Bx} and θ_{kB}. In particular, we first studied the deviation of the k vector from the magnetic field in a coordinate system defined by the magnetic field and the x_{GSE} direction. This coordinate system is illustrated in the left-hand panel of Figure 7. The **X** direction is aligned to the magnetic field and is defined to point upstream. The **Z** direction lies perpendicular to the plane defined by x_{GSE} and the magnetic field. **Y**
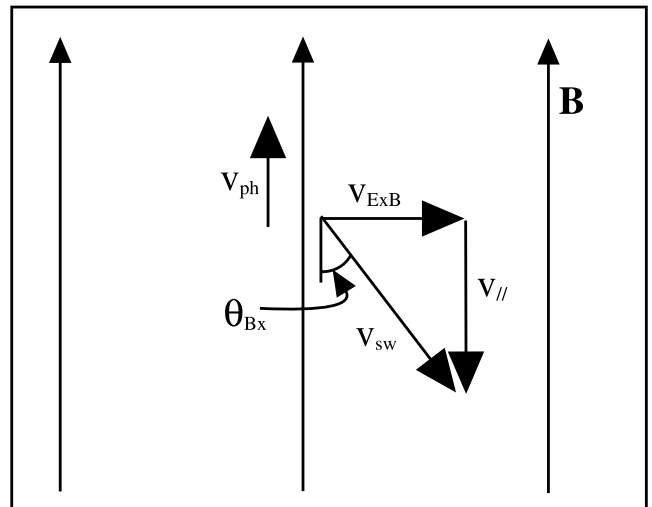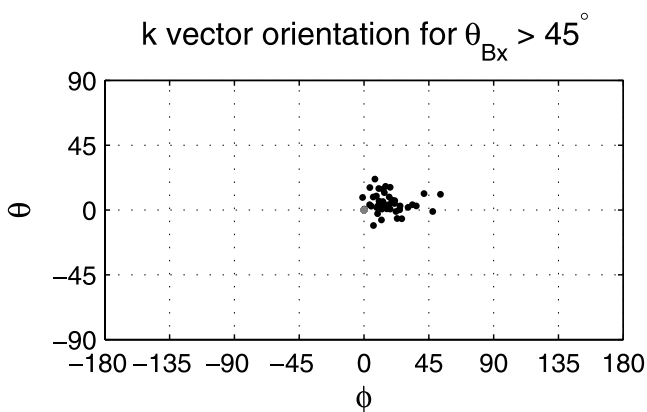

Figure 6. Illustration of convection. The solar wind velocity can be decomposed into parallel, $v_{\parallel}$, and perpendicular, $v_{E \times B}$, components relative to the magnetic field **B**. The waves are shown to propagate with velocity $\mathbf{v_{ph}}$. Since the solar wind is essentially aligned to the x_{GSE} direction, the magnetic field cone angle, θ_{Bx}, controls the magnitude of $v_{E \times B}$. The cone angle is defined to be "small" when $v_{E \times B} < v_{ph}$. In these circumstances, it is assumed that the effects of wave convection across field lines are minimised.
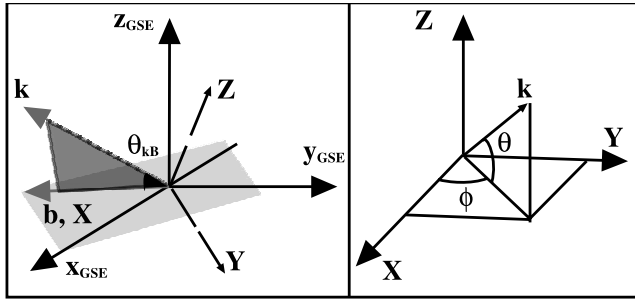
Figure 7. The left-hand panel shows the coordinate system [**X Y Z**] used when the magnetic field cone angle is large. **X** is aligned to the magnetic field (forced to point upstream). The **Z** direction is perpendicular to the plane defined by the magnetic field and $\mathbf{x}_{GSE}$, and **Y** = **Z** × **X**. The right-hand panel shows how the spherical polar angles ϕ and θ are defined in the new coordinate system.

completes a right-handed triple [**X Y Z**], and $\mathbf{x}_{GSE}\cdot\mathbf{Y} > 0$. Each unit k vector was transformed into this coordinate system and then converted from Cartesian into spherical polar coordinates [ϕ θ]. Here ϕ is the azimuthal angle in the [**X Y**] plane and θ is the elevation out of this plane in the +**Z** direction, as illustrated in the right-hand panel of Figure 7. The **X** direction points along $\phi = 0$, $\theta = 0$. If ϕ is positive, the k vector is rotated toward the Sun-Earth line.

[28] Figure 8 shows the spherical angles of the unit k vectors in this coordinate system for samples where $\theta_{Bx} > 45°$. The error in the location of each point is of the order of a few degrees. Figure 8 shows that the k vectors are mainly confined to the region $\phi > 0$. This corresponds to deflections toward $\mathbf{x}_{GSE}$. The center of the point distribution is [ϕ θ] = [$17 \pm 11°$ $4 \pm 6°$], where the errors are the standard deviations of the samples. There would appear to be an average systematic deflection of the k vectors away from the

ambient magnetic field, largely confined to the plane defined by the magnetic field and $\mathbf{x}_{GSE}$. We also observe a random deviation of the individual k vectors about the average.

[29] It is of interest to compare this result with the observations made when the magnetic field cone angle, θ_{Bx}, was small. If θ_{Bx} is small, we ought not to plot the data using the coordinate system defined in the left-hand panel of Figure 7, as the **Z** direction would not be well defined. Instead, a new coordinate system was constructed, based on the magnetic field and $\mathbf{z}_{GSE}$, as shown in the left-hand panel of Figure 9. The $\tilde{\mathbf{X}}$ direction is again aligned to the magnetic field and forced to point sunward. The $\tilde{\mathbf{Z}}$ direction is perpendicular to the $\tilde{\mathbf{X}}$ direction, in the plane defined by $\mathbf{z}_{GSE}$ and the magnetic field. Note that $\tilde{\mathbf{Z}}\cdot\mathbf{z}_{GSE} > 0$. The $\tilde{\mathbf{Y}}$ direction is defined such that [$\tilde{\mathbf{X}}$ $\tilde{\mathbf{Y}}$ $\tilde{\mathbf{Z}}$] forms a right-handed triple. The X directions of the two coordinate systems are aligned, and so the angular deflections in both cases are relative to the magnetic field.

[30] For the subset of 14 intervals where θ_{Bx} was small, the unit k vectors were transformed into this coordinate system and then converted into spherical polar coordinates. Here $\tilde{\phi}$, the azimuthal angle in the [$\tilde{\mathbf{X}}$ $\tilde{\mathbf{Y}}$] plane, and $\tilde{\theta}$, the elevation out of this plane in the $\tilde{\mathbf{Z}}$ direction, for each sample are shown in Figure 10. (The $\tilde{\mathbf{X}}$ direction again points along $\tilde{\phi} = 0$, $\tilde{\theta} = 0$.) Although there is a significant difference between individual unit k vectors and the magnetic field, there is no preferred direction for the deflection of each k vector. The centroid of the points is located at [$\tilde{\phi}$, $\tilde{\theta}$] = [$2°$ $0°$]. The data were tested to see if there was any dependence on the location of observation (above or below the ecliptic, dawn, or dusk flank), but no trends were apparent.

[31] To investigate this in more detail, the angles between the unit k vectors and unit magnetic field vectors were calculated for different ranges of θ_{Bx}. For each sample, the polar angles ϕ and θ were calculated in the [**X Y Z**] coordinate system (based on the magnetic field and $\mathbf{x}_{GSE}$, shown on the left of Figure 7). Figure 11 shows two two-dimensional histograms summarizing the data. The left-hand side of Figure 11 shows a two-dimensional histogram

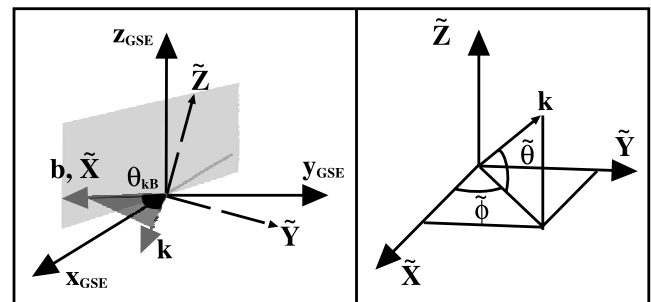### k vector orientation for $\theta_{Bx} > 45°$

Figure 8. The orientations of k vectors for 45 samples of quasi-monochromatic ULF wave activity where the angle between the magnetic field and the x GSE direction >45° are shown. The angles are the polar angles in the coordinate system defined in Figure 7. The plot is centered on the magnetic field. There is a systematic deviation in the ϕ angle, i.e., in the plane defined by the magnetic field and the $\mathbf{x}_{GSE}$, or solar wind vector. The black cross marks the average elevation and azimuth of the sample.

Figure 9. The left panel shows the coordinate system [$\tilde{\mathbf{X}}$ $\tilde{\mathbf{Y}}$ $\tilde{\mathbf{Z}}$] used when the magnetic field cone angle is small. The $\tilde{\mathbf{X}}$ direction is aligned to the magnetic field, the $\tilde{\mathbf{Z}}$ direction lies in the plane defined by the magnetic field and the $\mathbf{z}_{GSE}$ direction, and the $\tilde{\mathbf{Y}}$ direction is chosen such that [$\tilde{\mathbf{X}}$ $\tilde{\mathbf{Y}}$ $\tilde{\mathbf{Z}}$] is a right-handed triple. The right-hand panel shows how the spherical polar angles $\tilde{\phi}$ and $\tilde{\theta}$ are defined in the new coordinate system.
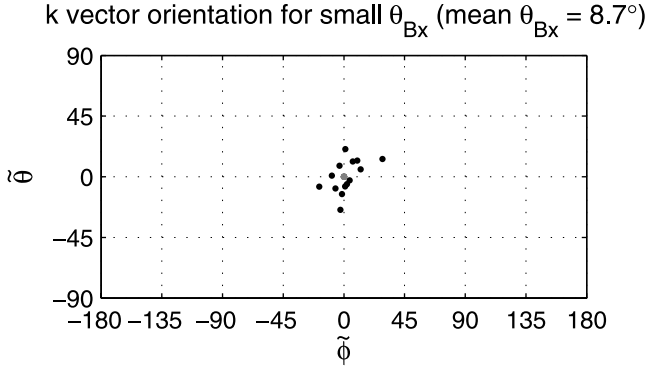
Figure 10. Orientation of k vectors for small θ_{Bx}. The data plotted here correspond to those samples where the convective component of the solar wind is less than the wave phase speed. There are 14 samples that satisfied this criterion, with an average cone angle of 8.9°. Each black point represents a k vector orientation relative to the magnetic field. The angles are the spherical coordinates in the coordinate system defined in Figure 9. The plot is centered on the magnetic field.

of the azimuthal angle ϕ and θ_{Bx}. The data were placed into 10° wide bins. The right-hand panel shows the corresponding histogram for the elevation angle θ. The majority of the data lie in the region $\phi > 0$ (i.e., rotated toward the Sun-Earth line) but are more evenly distributed about $\theta = 0$. Figure 12 is based on the same data but shows the average ϕ and θ angle in each θ_{Bx} bin. The left-hand panel again shows the average azimuth angle. The error bars are based on the standard deviations of the samples. Within errors, the average azimuth angle $\langle\phi\rangle$ is greater than zero for

the two largest θ_{Bx} bins. This appears to result from each k vector being deflected toward positive ϕ. The right-hand panel shows the average elevation. Except for the $50° < \theta_{Bx} \leq 60°$ bin, the average elevation angle is not significantly different from zero; no trend is apparent.

[32] Returning to the convection concept shown in Figure 6, thus far we have examined those intervals corresponding to $v_{E\times B}/v_{ph} < 1$. We will now extend these calculations. For each interval of wave activity, $v_{E\times B}/v_{ph}$ was calculated. This parameter characterizes the rate at which the wave packet is convected across magnetic field lines. A two-dimensional histogram was then constructed, based on $v_{E\times B}/v_{ph}$ and θ_{kB}. This histogram is shown in Figure 13. The data bins are 10° wide in θ_{kB} and 0.5 wide in $v_{E\times B}/v_{ph}$. As $v_{E\times B}/v_{ph}$ increases to ∼3, the maximum observed value of θ_{kB} increases, and the average value of θ_{kB} also increases. As mentioned above, even for $v_{E\times B}/v_{ph} < 1$, θ_{kB} is significantly nonzero. The two modal bins (n = 15 in each) are centered on $\theta_{kB} = 15.5°$ and $v_{E\times B}/v_{ph} = 2$.

[33] Finally, for completeness, we examined the dependence on the angles ϕ and θ (in the [**X Y Z**] coordinate system shown in the left-hand panel of Figure 7) as a function of $v_{E\times B}/v_{ph}$. The results of this analysis are shown in Figure 14. Again the majority of the data points exhibit positive ϕ, which corresponds to a deviation toward the Sun-Earth line. The points are more evenly distributed in θ. Overall a similar pattern is observed when compared to Figure 11.

4. Discussion

[34] We have examined the oblique propagation of the 30 s period foreshock waves. It would appear that there is a persistent deviation of the wave k vector from the magnetic
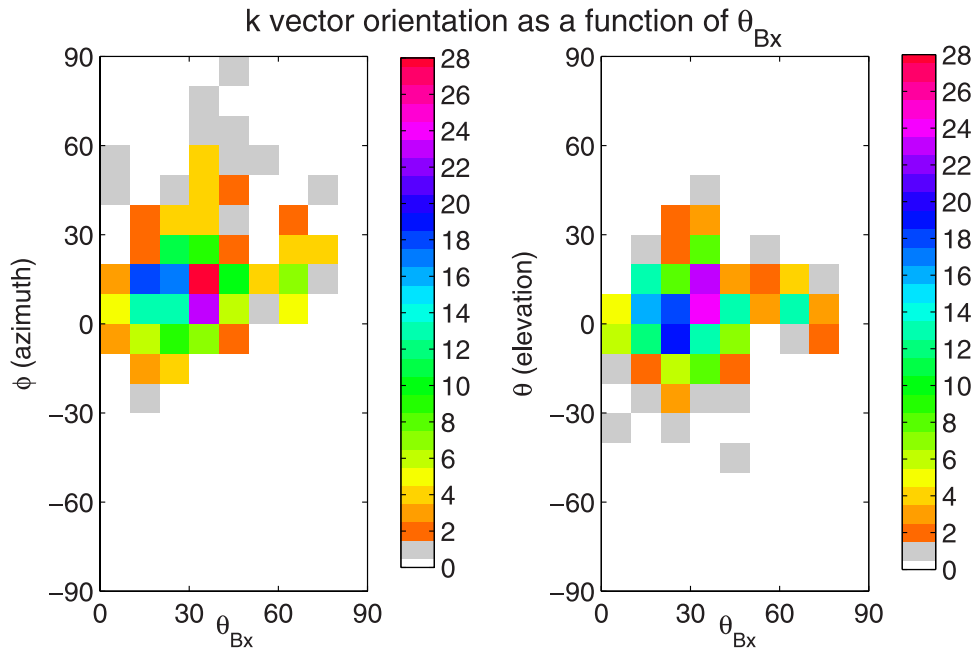
Figure 11. The left-hand panel shows a two-dimensional histogram of ϕ, the azimuth spherical polar angle in the [**X Y Z**] coordinate system, and θ_{Bx}. The right-hand panel shows the corresponding two-dimensional histogram for θ.
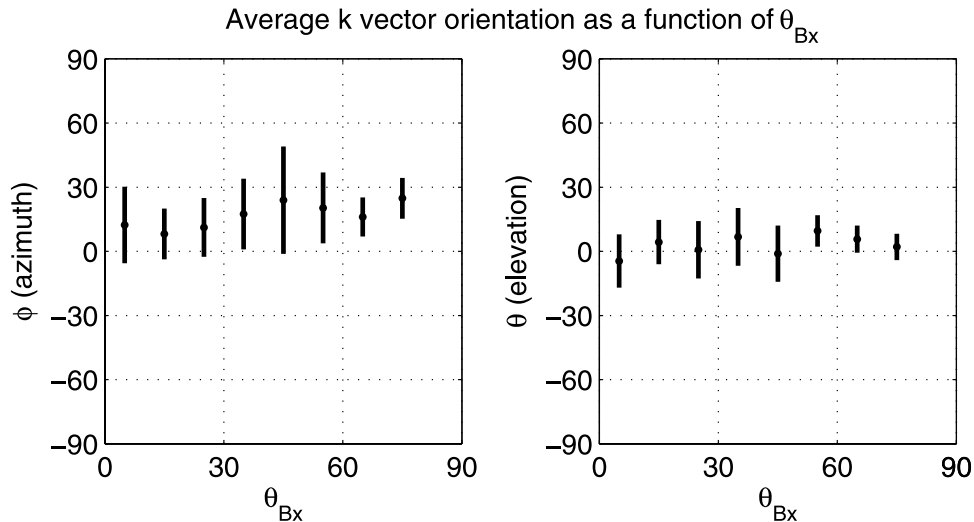
Figure 12. The left- and right-hand panels show the average ϕ and θ angles for different ranges of θ_{Bx} respectively. The error bars are constructed from the standard deviations of the samples. These data are also shown in Figure 11.

field. This is consistent with indications from previous case studies of such waves [*Hoppe et al.*, 1981; *Eastwood et al.*, 2002; *Eastwood et al.*, 2004]. Over the whole data set, the average θ_{kB} was found to be $20.9 \pm 14.1°$. There were 45 samples found where $\theta_{Bx} > 45°$, with $\theta_{kB} = 19.5 \pm 10.7°$. For these observations made when the IMF cone angle was large, the k vectors appeared to be shifted to more positive ϕ angles (Figure 8). When the IMF cone angle is small, such that the $\mathbf{E} \times \mathbf{B}$ component of the solar wind is less than the phase speed of the waves in the plasma rest frame, the average θ_{kB} was found to be $12.9 \pm 7.1°$. Hence the 30 s waves are still observed to propagate obliquely under radial IMF. Investigation of the orientation of these k vector samples relative to the magnetic field did not reveal any preferred direction for their deflection from the magnetic field (Figure 10). Each individual observation is subject to experimental error; this error is of the order of a few degrees.

[35] The dependence of the observations on θ_{kB} and $v_{E \times B}/v_{ph}$ was also studied in more detail. Plotting the data in a coordinate system based on the magnetic field and x_{GSE}, it was found that most waves were deflected to positive ϕ (i.e., toward the x_{GSE} direction in the x_{GSE}-B plane). With respect to θ_{kB}, it was found that the mean value of ϕ became significantly nonzero for large θ_{kB}. Similar behavior was observed for the dependence on $v_{E \times B}/v_{ph}$. We note that $v_{E \times B} = v_{sw} \times \sin\theta_{Bx}$, and so the qualitative consistency in the behavior of θ_{kB} as a function of the two parameters is perhaps to be expected.

[36] We note that the deflection of k vectors in the x_{GSE}-B plane is a qualitative property of the mechanism proposed by *Hada et al.* [1987] to explain the production of shocklets and discrete wave packets in the diffuse ion foreshock. It is also discussed by *Scholer et al.* [1993], in the context of gradients in the density of backstreaming ions, where the net effect of the backstreaming density gradient parallel to the shock normal is to refract the waves in the x_{GSE}-B plane. The waves examined here are typically observed in conjunction with gyrating and intermediate backstreaming ions. As the waves grow, they are convected across field lines

that are connected to reducing θ_{Bn} at the shock and significantly different beam properties [*Edmiston et al.*, 1982; *Tanaka et al.*, 1983; *Skadron et al.*, 1988]. More simulation work is required to determine how the change in beam properties alters the wave propagation.

[37] Each measurement of the wave propagation direction is an average over several wave cycles. This average can be considered as being taken at an effectively random time in the beam interaction. It would be of interest to conduct simulations using the observed plasma properties to initialize the system and to compare the behavior of a randomly selected point in the simulation grid with the observed data. It would also be of interest to see if the magnitude of the observed θ_{kB} can be reproduced by simulations initialized using the observed plasma parameters.
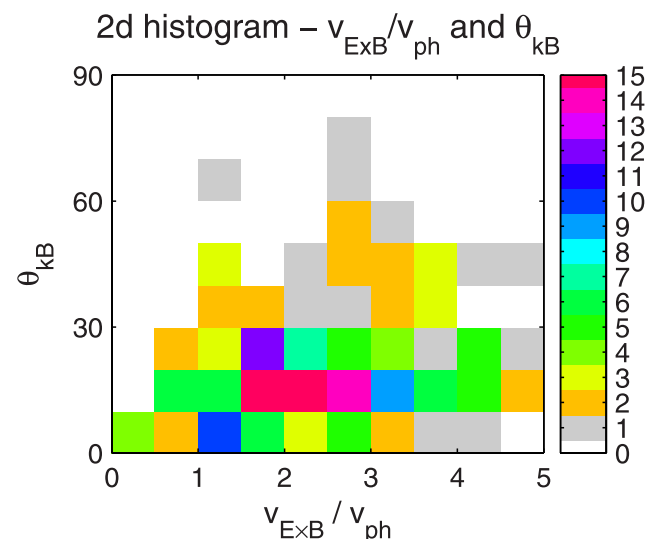
Figure 13. Two-dimensional histogram of θ_{kB} and $v_{E \times B}/v_{ph}$. The bin widths are $10°$ and 0.5, respectively. The color scale is used to represent the number density in each bin.
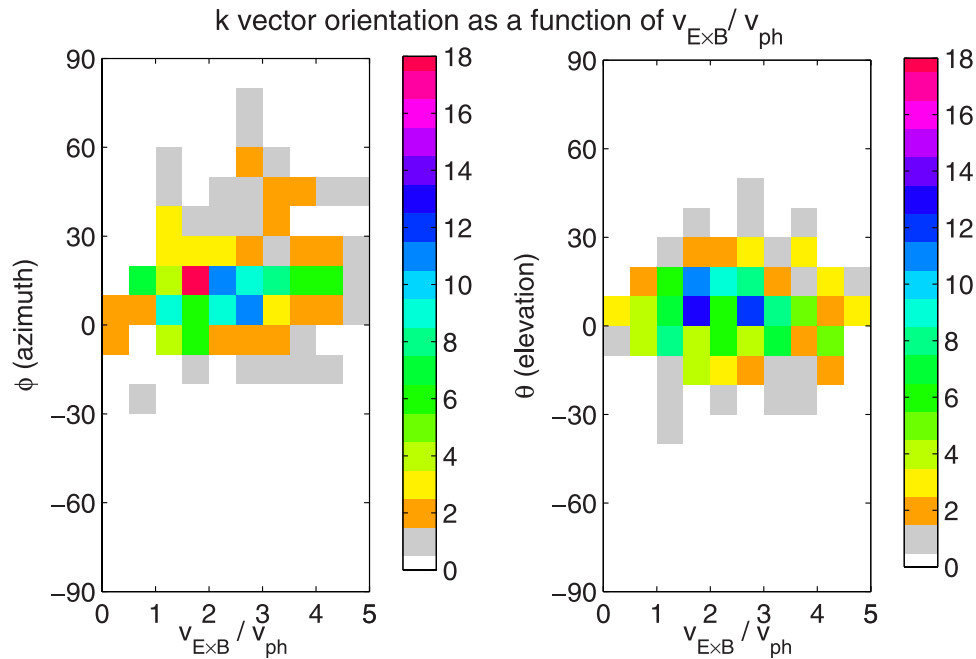
Figure 14. The left-hand panel shows a two-dimensional histogram of ϕ, the azimuth spherical polar angle in the [**X Y Z**] coordinate system, and $v_{E\times B}/v_{ph}$. The right-hand panel shows the corresponding two-dimensional histogram for θ.

[38] Other sources of variability may also play an important role. For example, the solar wind is time variable, and the shock is a nonstationary structure. This means that the particle input processes to the foreshock will not be time stationary, perhaps leading to transient changes in backstreaming particle fluxes. Variation of the IMF orientation will also lead to temporal changes in the morphology of the foreshock, and it is not clear how the foreshock "remembers" the time history of IMF variation. It has also been found that internal boundaries marking the onset of ULF wave activity and the location of intermediate and gyrating populations are ill-defined [*Le and Russell*, 1992; *Meziane and d'Uston*, 1998]. This combination of effects is likely to introduce inhomogeneities into the foreshock, which may have to be properly accounted for in order to understand these observations.

5. Conclusions

[39] In this paper we have presented experimental data concerning the problem of oblique ULF wave propagation in the foreshock. While this feature is well known qualitatively, particularly when manifested as compressive and steepening waves, there have been few experimental studies, especially when compared to the very extensive numerical investigations that have been published. Furthermore, specific experimental studies have concentrated on the properties of shocklets and discrete wave packets [*Hoppe et al.*, 1981; *Elaoufir et al.*, 1990]. Here we have examined the oblique propagation of 30 s period quasi-monochromatic waves. Previous to Cluster, the oblique propagation of these waves was reported in a limited number of case studies [*Hoppe and Russell*, 1983; *Eastwood et al.*, 2002, 2004].

[40] It has been found that these waves are persistently observed to propagate obliquely to the field, with $\theta_{kB} = 21 \pm$

14°. Oblique propagation is observed under "radial" IMF conditions, when θ_{Bx} is small. When the IMF cone angle is large, a systematic deviation of the wave k vectors toward positive azimuthal angles, in the plane defined by the x GSE direction and the magnetic field, together with a random deviation of the k vectors about the average is observed.

[41] The exact cause of the oblique propagation is unclear. The waves examined here are typically observed in association with intermediate or gyrophase bunched ion distributions, and so models examining the production of shocklets and discrete wave packets in the presence of diffuse ion distributions do not directly apply. Further simulation work is required to establish whether an analogous model can be used to explain these observations. Although recent two-dimensional simulations have reported the existence of oblique propagating modes [*Hellinger and Mangeney*, 1999; *Wang and Lin*, 2003], further work is required to establish quantitative consistency between these simulations and the experimental results presented here. In particular, we feel it is important to now establish if simulations can be conducted that reproduce the observed θ_{kB} given the observed plasma parameters (e.g., beam density, beam speed, background plasma beta, etc.).

[42] Furthermore, it may be necessary to incorporate more details of the foreshock into numerical and theoretical studies. In particular, the shock location is time variable and this, coupled with variations in upstream conditions, may introduce similarly time-dependent behavior in backstreaming beam speeds, fluxes, etc. This would lead to inhomogeneities in the superthermal population. Gradients in the density of the energetic particle flux may also play a role closer to the quasi-parallel shock. It has been shown in two-dimensional simulations that gradients in the backstreaming particle density can refract wave vectors [*Scholer et al.*, 1993]. In addition, the foreshock is inherently three-

dimensional, and two-dimensional models of the shock/foreshock system may prove unable to fully reproduce observed behavior. It may also be of interest to simulate the cyclotron interaction with a multicomponent core and beam to account for He^{++} observed in diffuse distributions.

[43] This work can be extended in a number of ways. Further work has been projected looking at the dependence of other wave parameters on θ_{kB}. In particular, it is of interest to examine the wave amplitude and to see if larger amplitude waves, which are presumably more developed, have different propagation properties. Although when this survey was carried out, we made it as complete as was then possible, it may not adequately represent all upstream conditions equally. A larger sample of observations would help to confirm these results by providing a more complete survey of all upstream conditions. As more data is accumulated in the Cluster archive, this will become possible. This study could also be extended to include shocklets and discrete wave packets. It is possible to use the techniques presented here in combination with the Cluster data set to identify their properties. In particular, the orientation of the shocklets can be studied directly using Cluster. Such an analysis could then be compared to the results presented here, and used to see if, for example, there is an increase in θ_{kB} as specifically predicted by the theory of Hada et al. [1987]. It would also be of interest to quantitatively examine the properties of shocklets and discrete wave packets when the IMF is radial. Finally, progress is also anticipated by more closely comparing these observations with the results of two- and three-dimensional simulations. For example, simulations could be used to generate synthetic data that might then undergo a Cluster-type multispacecraft analysis. Such an approach would allow a more stringent comparison of the observations and simulations to be made.

References

Akimoto, K., D. Winske, T. G. Onsager, M. F. Thomsen, and S. P. Gary (1991), Steepening of parallel propagating hydromagnetic waves into magnetic pulsations: A simulation study, *J. Geophys. Res.*, *96*, 17,599–17,607.

Akimoto, K., D. Winske, S. P. Gary, and M. F. Thomsen (1993), Nonlinear evolution of electromagnetic ion beam instabilities, *J. Geophys. Res.*, *98*, 1419–1433.

Balogh, A., C. M. Carr, M. H. Acuña, M. W. Dunlop, T. J. Beek, P. Brown, K.-H. Fornacon, E. Georgescu, K.-H. Glassmeier, J. Harris, G. Mussman, T. M. Oddy, and K. Schwingenschuh (2001), The Cluster magnetic field investigation: Overview of inflight performance and initial results, *Ann. Geophys.*, *19*, 1207–1217.

Barnes, A. (1970), Theory of generation of bow-shock-associated hydromagnetic waves in the upstream interplanetary medium, *Cosmic Electrodyn.*, *1*, 90–114.

Bendat, J. S., and A. G. Piersol (1986), *Random Data Analysis and Measurement Procedures*, John Wiley, Hoboken, N. J.

Bonifazi, C., and G. Moreno (1981), Reflected and diffuse ions backstreaming from the Earth's bow shock: 2. Origin, *J. Geophys. Res.*, *86*, 4405–4413.

Burgess, D. (1997), What do we really know about upstream waves?, *Adv. Space Res.*, *20*, (4/5)673–(4/5)682.

Daughton, W., and S. P. Gary (1998), Electromagnetic proton/proton instabilities in the solar wind, *J. Geophys. Res.*, *103*, 20,613–20,620.

Eastwood, J. P., A. Balogh, M. W. Dunlop, T. S. Horbury, and I. Dandouras (2002), Cluster observations of fast magnetosonic waves in the terrestrial foreshock, *Geophys. Res. Lett.*, *29*(22), 2046, doi:10.1029/2002GL015582.

Eastwood, J. P., A. Balogh, E. A. Lucek, C. Mazelle, and I. Dandouras (2003), On the existence of Alfvén waves in the terrestrial foreshock, *Ann. Geophys.*, *21*, 1457–1465.

Eastwood, J. P., A. Balogh, C. Mazelle, I. Dandouras, and H. Rème (2004), Oblique propagation of 30 s period fast magnetosonic foreshock waves: A Cluster case study, *Geophys. Res. Lett.*, *31*, L04804, doi:10.1029/2003GL018897.

Eastwood, J. P., A. Balogh, E. A. Lucek, C. Mazelle, and I. Dandouras (2005), Quasi-monochromatic ULF foreshock waves as observed by the four-spacecraft Cluster mission: 1. Statisical properties, *J. Geophys. Res.*, *110*, A11219, doi:10.1029/2004JA010617.

Edmiston, J. P., C. F. Kennel, and D. Eichler (1982), Escape of heated ions upstream of quasi-parallel shocks, *Geophys. Res. Lett.*, *9*, 531–534.

Elaoufir, J. A., A. Mangeney, T. Passot, C. C. Harvey, and C. T. Russell (1990), Large amplitude MHD waves in the Earth's proton foreshock, *Ann. Geophys.*, *8*, 297–307.

Escoubet, C. P., M. Fehringer, and M. L. Goldstein (2001), The Cluster mission, *Ann. Geophys.*, *19*, 1197–1200.

Fairfield, D. H. (1969), Bow shock associated waves observed in the far upstream interplanetary medium, *J. Geophys. Res.*, *74*, 3541–3553.

Fuselier, S. A. (1994), Suprathermal ions upstream and downstream from the Earth's bow shock, in *Solar Wind Sources of Magnetospheric Ultra-Low-Frequency Waves*, Geophys. Monogr. Ser., vol. 81, edited by M. J. Engebretson, K. Takahashi, and M. Scholer, pp. 107–119, AGU, Washington, D. C.

Fuselier, S. A. (1995), Ion distributions in the Earth's foreshock upstream from the bow shock, *Adv. Space Res.*, *15*, (8/9)43–(8/9)52.

Fuselier, S. A., M. F. Thomsen, J. T. Gosling, S. J. Bame, and C. T. Russell (1986), Gyrating and intermediate ion distributions upstream from the Earth's bow shock, *J. Geophys. Res.*, *91*, 91–99.

Gary, S. P. (1993), *Theory of Space Plasma Microinstabilities*, Cambridge Univ. Press, New York.

Gary, S. P., J. T. Gosling, and D. W. Forslund (1981), The electromagnetic ion beam instability upstream of the Earth's bow shock, *J. Geophys. Res.*, *86*, 6691–6696.

Gosling, J. T., M. F. Thomsen, S. J. Bame, W. C. Feldman, G. Paschmann, and N. Sckopke (1982), Evidence for specularly reflected ions upstream from the quasi-parallel shock, *Geophys. Res. Lett.*, *9*, 1333–1336.

Greenstadt, E. W., G. Le, and R. J. Strangeway (1995), ULF waves in the foreshock, *Adv. Space Res.*, *15*, (8/9)71–(8/9)84.

Gurgiolo, C., G. K. Parks, and B. H. Mauk (1983), Upstream gyrophase bunched ions: A mechanism for creation at the bow shock and the growth of velocity space structure through gyrophase mixing, *J. Geophys. Res.*, *88*, 9093–9100.

Hada, T., C. F. Kennel, and T. Terasawa (1987), Excitation of compressional waves and the formation of shocklets in the Earth's foreshock, *J. Geophys. Res.*, *92*, 4423–4435.

Hellinger, P., and A. Mangeney (1999), Electromagnetic ion beam instabilities: Oblique pulsations, *J. Geophys. Res.*, *104*, 4669–4680.

Hoppe, M. M., and C. T. Russell (1983), Plasma rest frame frequencies and polarizations of the low-frequency upstream waves: ISEE 1 and 2 observations, *J. Geophys. Res.*, *88*, 2021–2028.

Hoppe, M. M., C. T. Russell, L. A. Frank, T. E. Eastman, and E. W. Greenstadt (1981), Upstream hydromagnetic waves and their association with backstreaming ion populations: ISEE 1 and 2 observations, *J. Geophys. Res.*, *86*, 4471–4492.

Hoshino, M., and T. Terasawa (1985), Numerical study of the upstream wave excitation mechanism: 1. Nonlinear phase bunching of beam ions, *J. Geophys. Res.*, *90*, 57–64.

Krauss-Varban, D., and N. Omidi (1993), Propagation characteristics of waves upstream and downstream of quasi-parallel shocks, *Geophys. Res. Lett.*, *20*, 1007–1010.

Kucharek, H., M. Scholer, and A. P. Matthews (2000), Three-dimensional simulation of the electromagnetic ion/ion beam instability: Cross field diffusion, *Nonlinear Proc. Geophys.*, *7*, 167–172.

Le, G., and C. T. Russell (1992), A study of ULF wave foreshock morphology - I: ULF foreshock boundary, *Planet. Space Sci.*, *40*, 1203–1213.

Le, G., and C. T. Russell (1994), The morphology of ULF waves in the Earth's foreshock, in *Solar Wind Sources of Magnetospheric Ultra-Low-Frequency Waves*, Geophys. Monogr. Ser., vol. 81, edited by M. J. Engebretson, K. Takahashi, and M. Scholer, pp. 87–98, AGU, Washington, D. C.

Maksimovic, M., S. D. Bale, T. S. Horbury, and M. André (2003), Bow shock motions observed with CLUSTER, *Geophys. Res. Lett.*, *30*(7), 1393, doi:10.1029/2002GL016761.

Mazelle, C., D. Le Quéau, and K. Meziane (2000), Nonlinear wave-particle interaction upstream from the Earth's bow shock, *Nonlinear Proc. Geophys.*, *7*, 185–190.

Mazelle, C., et al. (2003), Production of gyrating ions from nonlinear wave-particle interaction upstream from the Earth's bow shock: A case study from Cluster-CIS, *Planet. Space Sci.*, *51*, 785–795.

Meziane, K., and C. d'Uston (1998), A statistical study of the upstream intermediate ion boundary in the Earth's foreshock, *Ann. Geophys.*, *16*, 125–133.

Meziane, K., et al. (1997), Wind observations of gyrating-like ion distributions and low frequency waves upstream from the Earth's bow shock, *Adv. Space Res.*, *20*, (4/5)703–(4/5)706.

Meziane, K., C. Mazelle, R. P. Lin, D. Le Quéau, D. E. Larson, G. K. Parks, and R. P. Lepping (2001), Three-dimensional observations of gyrating ion distributions far upstream from the Earth's bow shock and their association with low-frequency waves, *J. Geophys. Res.*, *106*, 5731–5742.

Möbius, E., et al. (2001), Observations of the spatial and temporal structure of field-aligned beam and gyrating ring distributions at the quasi-perpendicular bow shock with Cluster CIS, *Ann. Geophys.*, *19*, 1411–1420.

Narita, Y., K.-H. Glassmeier, S. Schafer, U. Motschmann, K. Sauer, I. Dandouras, K.-H. Fornacon, E. Georgescu, and H. Rème (2003), Dispersion analysis of ULF waves in the foreshock using cluster data and the wave telescope technique, *Geophys. Res. Lett.*, *30*(13), 1710, doi:10.1029/2003GL017432.

Omidi, N., and D. Winske (1990), Steepening of kinetic magnetosonic waves into shocklets: Simulations and consequences for planetary shocks and comets, *J. Geophys. Res.*, *95*, 2281–2300.

Omidi, N., and D. Winske (1998), Subcritical dispersive shock waves upstream of planetary bow shocks and at comet Giacobini-Zinner, *Geophys. Res. Lett.*, *15*, 1303–1306.

Paschmann, G., N. Sckopke, S. J. Bame, J. R. Asbridge, J. T. Gosling, C. T. Russell, and E. W. Greenstadt (1979), Association of low frequency waves with suprathermal ions in the upstream solar wind, *Geophys. Res. Lett.*, *6*, 209–212.

Peredo, M., J. A. Slavin, E. Mazur, and S. A. Curtis (1995), Three-dimensional position and shape of the bow shock and their variation with Alfvénic, sonic and magnetosonic Mach numbers and interplanetary magnetic field orientation, *J. Geophys. Res.*, *100*, 7907–7916.

Rème, H., et al. (2001), First multispacecraft ion measurements in and near the Earth's magnetosphere with the identical Cluster ion spectrometry (CIS) experiment, *Ann. Geophys.*, *19*, 1303–1354.

Scholer, M. (1995), Interaction of upstream diffuse ions with the solar wind, *Adv. Space Res.*, *15*, (8/9)125–(8/9)135.

Scholer, M., M. Fujimoto, and H. Kucharek (1993), Two-dimensional simulations of supercritical quasi-parallel shocks: Upstream waves, downstream waves, and shock re-formation, *J. Geophys. Res.*, *98*, 18,971–18,984.

Schwartz, S. J. (1998), Shock and discontinuity normals, Mach numbers and related parameters, in *Analysis Methods for Multi-Spacecraft Data*, edited by G. Paschmann and P. W. Daly, pp. 249–270, Int. Space Sci. Inst., Bern, Switzerland.

Schwartz, S. J., and D. Burgess (1984), On the theoretical/observational comparison of field-aligned ion beams in the Earth's foreshock, *J. Geophys. Res.*, *89*, 2381–2384.

Skadron, G., R. D. Holdaway, and M. A. Lee (1988), Formation of the wave compressional boundary in the Earth's foreshock, *J. Geophys. Res.*, *93*, 11,354–11,362.

Song, P., and C. T. Russell (1999), Time series data analyses in space plasmas, *Space Sci. Rev.*, *87*, 387–463.

Sonnerup, B. U. Ö. (1969), Acceleration of particles reflected at a shock front, *J. Geophys. Res.*, *74*, 1301–1304.

Tanaka, M., C. C. Goodrich, D. Winske, and K. Papadopoulos (1983), A source of the backstreaming ion beams in the foreshock region, *J. Geophys. Res.*, *88*, 3046–3054.

Thomsen, M. F. (1985), Upstream suprathermal ions, in *Collisionless Shocks in the Heliosphere: Reviews of Current Research*, Geophys. Monogr. Ser., vol. 35, edited by B. T. Tsurutani and R. G. Stone, 253–270, AGU, Washington, D. C.

Thomsen, M. F., J. T. Gosling, S. J. Bame, and C. T. Russell (1985), Gyrating ions and large-amplitude monochromatic MHD waves upstream of the Earth's bow shock, *J. Geophys. Res.*, *90*, 267–273.

Treumann, R. A., and W. Baumjohann (1996), *Advanced Space Plasma Physics*, Imperial Coll. Press, London.

Wang, X. Y., and Y. Lin (2003), Generation of nonlinear Alfven and magnetosonic waves by beam-plasma interaction, *Phys. Plasmas*, *10*, 3528–3538.

Winske, D., and M. M. Leroy (1984), Diffuse ions produced by electromagnetic ion beam instabilities, *J. Geophys. Res.*, *89*, 2673–2688.

Winske, D., and K. B. Quest (1986), Electromagnetic ion beam instabilities: Comparison of one- and two-dimensional simulations, *J. Geophys. Res.*, *91*, 8789–8797.

————————

A. Balogh and E. A. Lucek, Space and Atmospheric Physics, Blackett Laboratory, Imperial College London, Prince Consort Road, London SW7 2BW, UK.

I. Dandouras and C. Mazelle, Centre d'Etude Spatiale des Rayonnements, Centre National de la Recherche Scientifique, 9 avenue du colonel Roche, F-31028 Toulouse, France.

J. P. Eastwood, Laboratory for Solar and Space Physics, Geospace Physics Branch, NASA Goddard Space Flight Center, Code 612.3, Greenbelt, MD 20771, USA. (jonathan.p.eastwood.1@gsfc.nasa.gov)